Research Article

DEVELOPMENT OF A NEW LINEAR DELTA ROBOT FOR THE FUSED DEPOSITION MODELLING PROCESS

J. Pattavanitch*
S. Panyaru

Department of Mechanical Engineering, Faculty of Engineering, Burapha University 169 Long-Hard Bangsaen Rd., Muang, Chonburi, 20131 Thailand

ABSTRACT:
This paper aims to explain the design and construction of a new linear delta robot for the fused deposition modelling (FDM) process. The kinematics of the robot, including the inverse and forward kinematics, are derived. These kinematics are used to determine the geometric parameters of the robot. The workspace of the designed robot is presented, and the robot performance is checked with the conditioning index (CI). The robot is tested to evaluate robot accuracy by repeatedly travelling to the required location. The actual travel paths of the robot are also investigated. The robot is equipped with a filament spool, extruder nozzle to fabricate physical objects by FDM process. The control system is computer-based. The control program is developed using a Visual Basic .NET framework. The program allows the user to control the robot and the process via a graphical user interface (GUI). The robot system is tested to create thin-wall objects with four different shapes which are square, cylindrical, square-based pyramid and rounded gear to illustrate the capability of the developed additive manufacturing system.

Keywords: *Linear delta robot, Fused deposition modelling, Additive manufacturing*

1. INTRODUCTION

In product development, prototypes must be created to visualise aspects such as shape, to inspect dimensions or sometimes to do physical testing before mass manufacturing. Many techniques are used to create prototypes, one of which is additive manufacturing (AM) or 3D printing. AM refers to a group of processes for fabricating physical objects directly from 3D computer-aided design (3D CAD) involving layer-by-layer stacking [1]. Thus, AM offers the opportunity of fabricating components without elaborate tooling.

There are several different methods of AM. The most widely used is a process known as fused deposition modelling (FDM), developed by Stratasys Inc. In the FDM process, filament-based material is fed into the heating element to melt the material and is then extruded through a nozzle. After deposition, the fused material solidifies and adheres to the preceding layer. Thus, a new layer is created. The nozzle keeps moving to deposit the subsequent layers until the process is completed.

Because the layers are formed using a mobile nozzle, the objects can be fabricated not only within a build chamber but also on any surface outside the confines of a build chamber, such as on a freeform surface [2] or pre-machined component faces [3, 4]. Another advantage of this process is that it is able to handle multiple printing heads to fabricate a component with different materials [5].

* Corresponding author: J. Pattavanitch
E-mail address: jitti@eng.buu.ac.th

The thermal extrusion process in the FDM process enables the use of various types of material, from traditional thermoplastic such as polylactic acid (PLA) and acrylonitrile butadiene styrene (ABS) to newer materials such as bioresorbable polymer [6], ceramics [7], metal [8] and composite material [9,10]. FDM is used to build parts for many applications ranging from large-scale components in the automotive [10] and aerospace industries [11] to micro-scale objects in medical applications [12].

Because the FDM process uses a mobile nozzle, it requires a mechanism to position the nozzle. There are several types of mechanisms designed for the FDM process, such as Cartesian, linear delta, polar and SCARA mechanisms. However, only the first two are currently available on the 3D printer market.

A Cartesian mechanism consists of three linear axes that are perpendicular to each other. The movement of an axis will not affect the other axes. With a Cartesian arrangement, the print nozzle moves on the X-Y plane and a print bed moves on the Z axis [13, 14] or the nozzle travels on the X-Z plane and a print bed moves on the Y axis [15].

In comparison, the linear delta mechanism uses parallelograms to manoeuver the nozzle. Therefore, the print bed is stationary and the print head is located in a 3D space [16, 17].

The Cartesian mechanism is of a simple design, resulting in ease of control. However, the operation speeds are rather low. This is because some of the moving components have to carry the motor and the components of other axes, resulting in increased time to accelerate or decelerate the mechanism's inertia. In contrast, the motors in a linear delta mechanism are mounted to the frame of the printer. Therefore, the weight and inertia of the moving parts is low. Consequently, the linear delta mechanism can operate at high speeds and accelerations.

Due to its high speed capability, a linear delta mechanism can be used not only in the conventional FDM process but also in curved layer fused deposition modelling (CLFDM) [18] in which the nozzle travels with various z-values rather than a fixed value during the creation of a layer. The main advantages of CLFDM are the improvement in surface smoothness and the strength of completed objects [19].

At the present time, linear delta 3D printers are available in the marketplace. However, the performance of the mechanism and how the accuracy of the printer is achieved are not detailed. Therefore, the aim of this paper is to describe the design and construction of a new linear delta robot that can be used to fabricate physical objects using the FDM process and to analyse the accuracy of the mechanism. A computer program to control and monitor the printer is also developed. Although the robots can be employed to fabricate components using CLFDM, the work herein focuses on conventional FDM.

2. LINEAR DELTA ROBOT CONFIGURATION

The configuration of the robot is illustrated in Fig. 1. The robot has three pairs of columns that are fixed on the base. Each pair of columns has a carriage that attaches to the end effector by two parallel arms of the same length via ball joints at each end. Consequently, the motion of the end effector is constrained to three translational degrees of freedom and is parallel to the base. Therefore, when carriages slide along the columns, the arms will transmit the movement to the effector, and the effector moves.
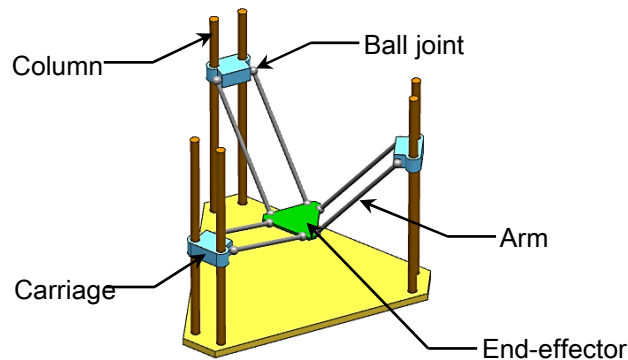

**Fig. 1.** Schematic of a delta robot.

3. KINEMATIC ANALYSIS OF DELTA ROBOT

The kinematic equations of the robot show the relationship between the position of the effector and that of each carriage. To analyse the kinematic equations, the robot configuration (Fig. 1) is reduced to a simple mechanism, as illustrated in Figs. 2 and 3.

Three pairs of columns are represented by three vertical cylinders, with their top ends denoted as A_i ($i =1, 2, 3$).The midpoint between two ball joints connecting on a carriage is denoted as B_i and the midpoint on the effector is denoted as P_i (see Fig. 2(a)). The arms have the length of L ($|\overrightarrow{P_i B_i}| = L$) (Fig. 2(b)).
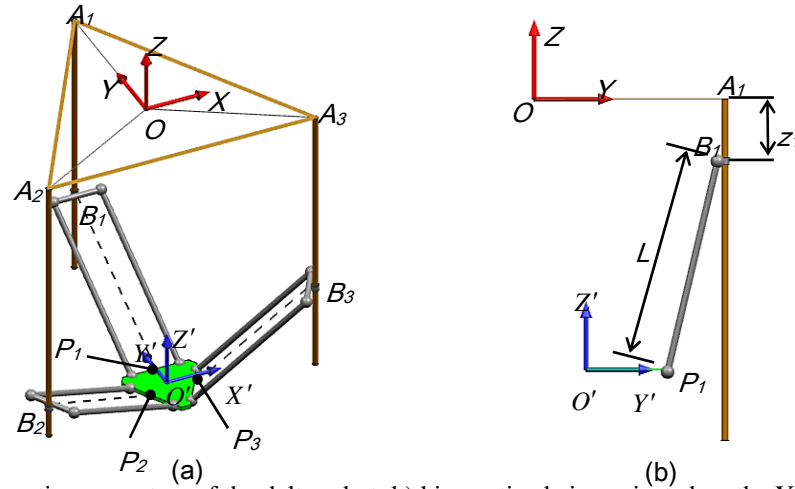
Fig. 2. a) Kinematic parameters of the delta robot; b) kinematic chain projected on the Y-Z plane.
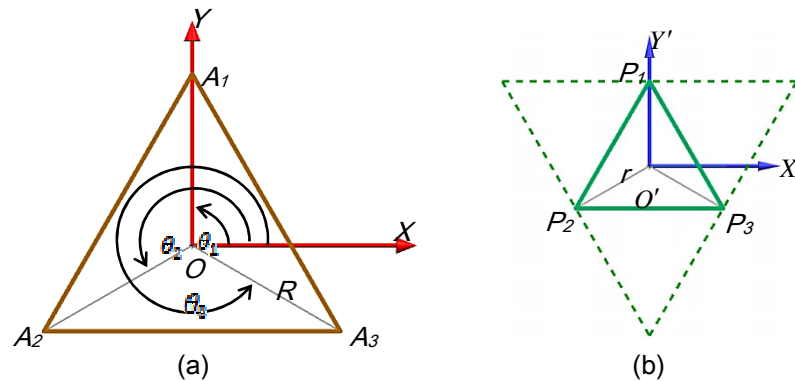
Fig. 3. a) Top view of the robot; b) top view of the end-effector.

To derive the kinematic model of the robot, two reference systems are defined in the analysis. The global reference system ($O-XYZ$) is located at the centre of the triangle ($A_1 A_2 A_3$) (Fig. 2(a)). The end effector reference ($O-X'Y'Z'$) is assigned to the centre of the triangle ($P_1 P_2 P_3$).

Assuming that the distance from the global reference (O) to A_i is R ($OA_1 = OA_2 = OA_3 = R$) (Fig. 3(a)) and the distance from the effector reference (O') to P_i is r ($O'P_1 = O'P_2 = O'P_3 = r$) (Fig. 3(b)).

Consider the loop $O - B_i - P_i - O'$ in Fig. 2(b); the vector-loop closure equation with respect to the global reference ($O-XYZ$) can be expressed as:

$$\overrightarrow{P_i B_i} = (\overrightarrow{O'P_i} + \overrightarrow{OO'}) - \overrightarrow{OB_i} \qquad (1)$$

The position of point O' and B_i with respect to the global reference (O) is:

$$\overrightarrow{OO'} = [x \quad y \quad z]^T \tag{2}$$

$$\overrightarrow{OB_i} = [R\cos\theta_i \quad R\sin\theta_i \quad z_i]^T \tag{3}$$

where $\theta_i = \dfrac{4i-1}{6}\pi$,

and the position of point P_i in the platform reference (O') can be represented as follows:

$$\overrightarrow{O'P_i} = [r\cos\theta_i \quad r\sin\theta_i \quad 0]^T \tag{4}$$

By substituting the position vectors (Eqs. (2) - (4)) into the vector-loop enclosure equation (Eq. (1)) and using constrain $\left|\overrightarrow{P_iB_i}\right| = L$, the kinematic equations of the robot can then be written as:

$$x^2 + (y+r-R)^2 + (z-z_1)^2 = L^2 \tag{5}$$

$$\left(x - \frac{\sqrt{3}}{2}(r-R)\right)^2 + \left(y - \frac{1}{2}(r-R)\right)^2 + (z-z_2)^2 = L^2 \tag{6}$$

$$\left(x - \frac{\sqrt{3}}{2}(R-r)\right)^2 + \left(y - \frac{1}{2}(r-R)\right)^2 + (z-z_3)^2 = L^2 \tag{7}$$

3.1 Inverse position kinematics

Inverse kinematics refers to the use of the kinematics equations to determine the relationship between the positions of the three carriages (z_i) on their columns and the location of the end effector. By rearranging Eqs (5) - (7), the variable z_i can be expressed as a function of the position (x, y, z) of the effector, as follows:

$$z_1 = z \pm \sqrt{L^2 - x^2 - (y-R+r)^2} \tag{8}$$

$$z_2 = z \pm \sqrt{L^2 - \left(x - \frac{\sqrt{3}}{2}(r-R)\right)^2 - \left(y - \frac{1}{2}(r-R)\right)^2} \tag{9}$$

$$z_3 = z \pm \sqrt{L^2 - \left(x - \frac{\sqrt{3}}{2}(R-r)\right)^2 - \left(y - \frac{1}{2}(r-R)\right)^2} \tag{10}$$

In this work, the sign $\pm$ in the equations is assumed to be positive.

3.2 Forward position kinematics

Forward kinematics involve solving kinematic equations to determine the position of the effector (x, y, z) when the positions of the three carriages (z_i) are specified. The forward kinematics equations are obtained by calculating the root of the following parameters:

$$E z^2 + F z + G = 0 \tag{11}$$

$$x = Az + B \tag{12}$$

$$y = Cz + D \tag{13}$$

where

$$A = \frac{(z_2 - z_3)}{\sqrt{3}(R - r)}, \quad B = \frac{(z_3^2 - z_2^2)}{2\sqrt{3}(R - r)},$$

$$C = \frac{2(z_2 - z_1) - \sqrt{3}(R - r)A}{3(R - r)}, \quad D = \frac{z_1^2 - z_2^2 - \sqrt{3}(R - r)B}{3(R - r)},$$

$$E = A^2 + C^2 + 1, \quad F = 2AB + 2CD - 2C(R - r) - 2z_1, \text{ and}$$

$$G = B^2 + D^2 - 2D(R - r) + (R - r)^2 + z_1^2 - L^2$$

3.3 Jacobian matrix and conditioning index

The Jacobian matrix is defined as the matrix that maps the relationship between the velocity of the effector and the vector of actuated joint rates [20]. The velocity equation of the robot can be obtained by differentiating the kinematic equation (Eqs. (5) - (7)) with respect to time, which is written into matrix form as:

$$\dot{\mathbf{v}} = \mathbf{J}\dot{\mathbf{u}} \tag{14}$$

where $\dot{\mathbf{v}}$ and $\dot{\mathbf{u}}$ are the vector velocities of the effector and carriages, which are

$$\dot{\mathbf{v}} = [\dot{x} \quad \dot{y} \quad \dot{z}]^T \tag{15}$$

and

$$\dot{\mathbf{u}} = [\dot{z}_1 \quad \dot{z}_2 \quad \dot{z}_3]^T \tag{16}$$

The Jacobian matrix ($\mathbf{J}$) of the robot can then be derived as follows:

.

$$
\mathbf{J} = \begin{bmatrix}
\dfrac{-x}{\sqrt{L^2 - x^2 - (y - R + r)^2}} & \dfrac{R - r - y}{\sqrt{L^2 - x^2 - (y - R + r)^2}} & 1 \\[3mm]
\dfrac{\frac{\sqrt{3}}{2}(r - R) - x}{\sqrt{L^2 - \left(x - \frac{\sqrt{3}}{2}(r - R)\right)^2 - \left(y - \frac{1}{2}(r - R)\right)^2}} & \dfrac{\frac{1}{2}(r - R) - y}{\sqrt{L^2 - \left(x - \frac{\sqrt{3}}{2}(r - R)\right)^2 - \left(y - \frac{1}{2}(r - R)\right)^2}} & 1 \\[3mm]
\dfrac{\frac{\sqrt{3}}{2}(R - r) - x}{\sqrt{L^2 - \left(x - \frac{\sqrt{3}}{2}(R - r)\right)^2 - \left(y - \frac{1}{2}(r - R)\right)^2}} & \dfrac{\frac{1}{2}(r - R) - y}{\sqrt{L^2 - \left(x - \frac{\sqrt{3}}{2}(R - r)\right)^2 - \left(y - \frac{1}{2}(r - R)\right)^2}} & 1
\end{bmatrix}
\tag{17}
$$

The conditioning index (CI) is used to evaluate the isotropy of the robot, which can be calculated as [21]:

$$
CI = \frac{1}{\left\| \mathbf{J}^{-1} \right\| \cdot \left\| \mathbf{J} \right\|}
\tag{18}
$$

where $\left\| \mathbf{J} \right\|$ is calculated as:

$$
\left\| \mathbf{J} \right\| = \sqrt{tr\left(\mathbf{J}^T \mathbf{W} \mathbf{J}\right)}; \quad \mathbf{W} = \frac{1}{n}\mathbf{I}
\tag{19}
$$

where n is the dimension of the Jacobian matrix, and $\mathbf{I}$ is the $n \times n$ identity matrix.

The CI has a value between 0 and 1. The robot is in its isotropy configuration if CI equals 1. When the CI equals 0, the robot is in its singularity, where the robot will be out of control.

4. WORKSPACE ANALYSIS

The values of the robot parameters—that is, L, R and r—are required to construct the robot. These parameters will affect not only the volume of the workspace but also the performance of the robot. In this work, the conditions to determine the robot parameters are that the robot has a workspace of 200 x 200 x 200 mm and, to ensure that the robot is far from singularity, the value of the CI within the workspace must not be less than 0.6.

By using an iteration technique, the value of the parameters are computed as L=350 mm, R=178 mm and r=30 mm. With these parameters, the reachable workspace of the robot is bigger than the required workspace (see Fig. 4(a)), and the minimum value of the CI within the workspace (represented in the rectangular area in Figs 4(b) to (d)) is 0.62, which is greater than that of the constraint value (0.60). The computed robot parameters satisfy the designed conditions. Therefore, the robot will be built using these parameters.
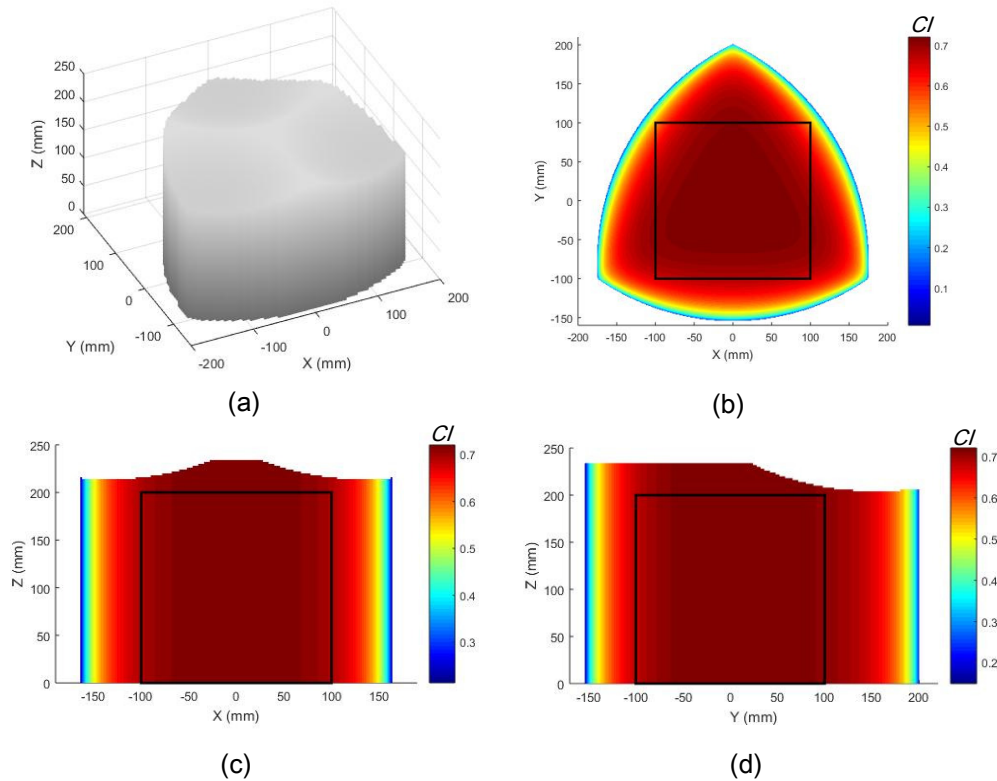
Fig. 4. a) The workspace of the robot; Distribution of *CI*: b) X-Y plane; c) X-Z plane; d) Y-Z plane.

5. HARDWARE DEVELOPMENT AND CONTROL SYSTEM

The designed robot uses a triangular frame to provide good balance and stability (see Fig. 5). The material for the top plate is aluminium alloy and that for the bottom plate is steel. Six shafts are fastened to the top and bottom plates. These shafts are made from steel to provide sufficient rigidity and to protect against frame distortions.

The arms of the robot are made of hollow stainless tube. Each arm has two parallel links connecting each carriage to the end effector via rod-end ball joints. The end effector is made of aluminium alloy and has a triangular shape.

A carriage is connected to a pair of shafts using linear bearings. Timing belts are attached to the carriages to actuate the carriages along the shafts. The motors to drive the timing belts are mounted at the bottom of the structure. All the drive motors are NEMA 23 stepper motors equipped with motor drivers with a resolution of 20,000 step/rev. These motors can produce high torques at high speeds.

The filament of the material is stored in a spool located on the top of the robot frame. A filament extrusion, which is a mechanism made up of a motor to rotate a toothed pinch wheel, is installed on the top of the robot frame. The extruder motors is NEMA 17 stepper motors equipped with motor drivers with a resolution of 1,600 step/rev. The extruder pulls the filament from its spool through a low-friction Teflon tube to the print head. The print head consists of a nozzle, a filament heater and a cooling fan. These components are fastened together at the centre of the effector.

When the filament is extruded through the heater and the nozzle, the molten filament is deposited on the build plate. The build plate is a heat plate covered by a glass plate. The plate is suspended on four adjustable spring bolts used to adjust the tilt of the bed to ensure the build surface is perfectly flat.

A limit switch is mounted at the upper end of a pair of columns to provide a setting point for the home position of the carriages and to prevent the carriages translate out of the robot.
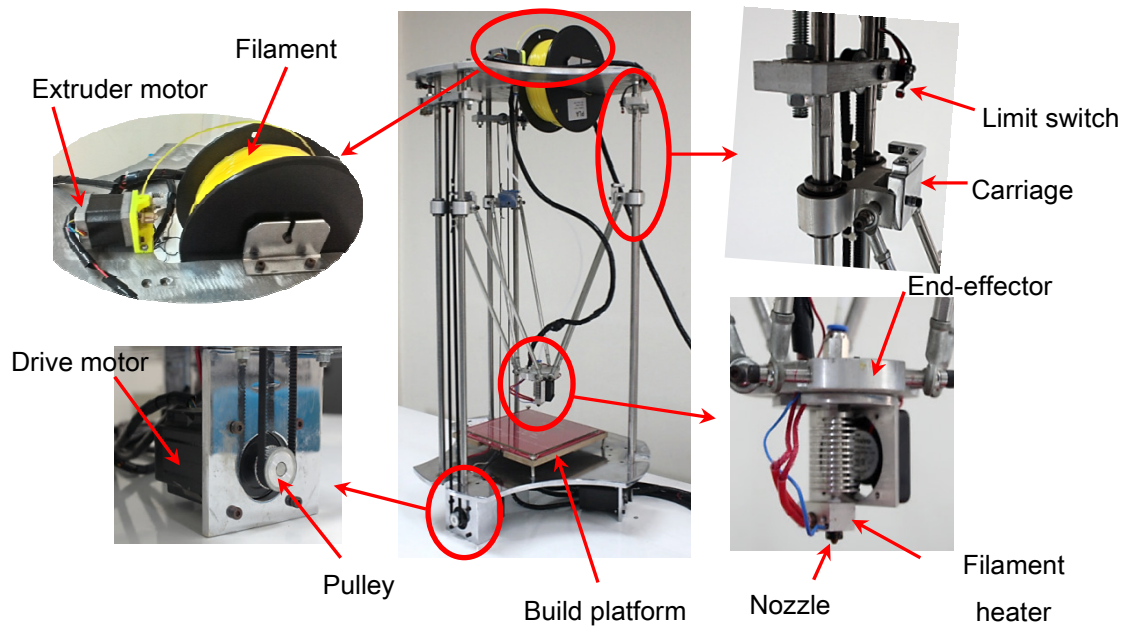
Fig. 5. The developed delta robot system.

A programmable logic controller (PLC) is used for the main controller of the robot because it has several digital inputs and outputs and is highly accurate in terms of timing the steps for the stepper motors. In addition, a PLC can process multiple tasks at the same time.

A diagram of the robot control system, which is computer-based, is shown in Fig. 6. The control program is written using a Visual Basic .NET framework. The program allows the user to control the robot via a GUI. To operate the robot system, the user inputs the paths of the nozzle as in the form of G-code, feed rate and the temperature of the build platform and filament heater. The program determines the number of pulse steps and the pulse frequency required to rotate the drive motors and the extruder motor, and it also converts the temperature values to hexadecimal format. These parameters are sent to the PLC via a serial communication port.

The PLC then generates electrical signals to turn all motors synchronously and creates a setting point for the temperature controllers so that the temperatures of the heat plate and the filament heater are at the required values during the building of objects. Two thermocouples, one at the filament heater and the other at the build plate, are used to send signals for each temperature controller.

As the robot is operating, the PLC sends the current values of the steps of the motors and of the current temperatures (in hexadecimal format) to the control program so that those parameters are converted to the current position of the nozzle and the current temperature of the building platform and the filament heater.
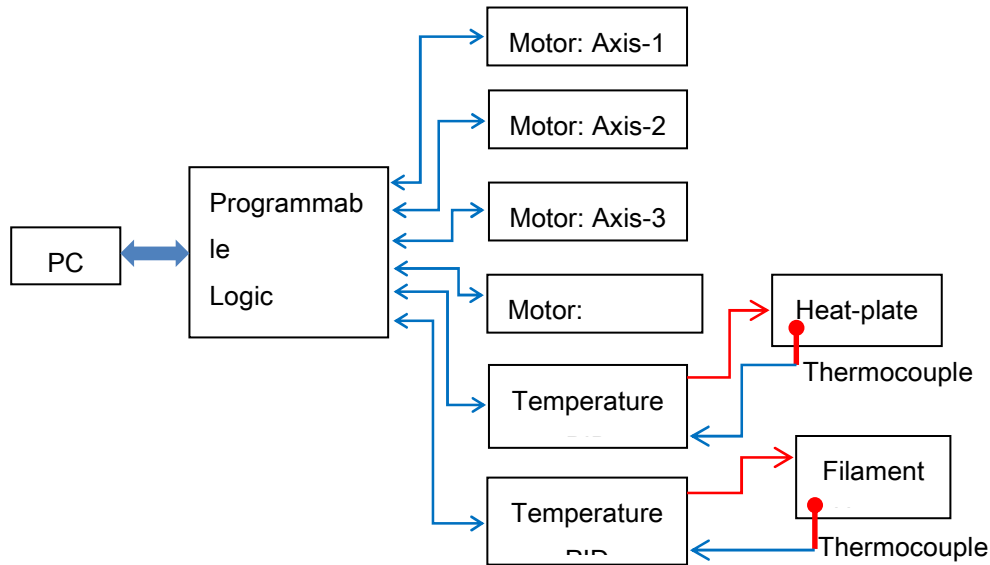
Fig. 6. Diagram of control system.

6. MOTION ANALYSIS

To investigate the accuracy of the robot, experiments in robot positioning were performed. The end effector of the robot was moved in the x, y and z directions, with linear travel paths at different distances and feed rates. The distances experimentally measured were compared with the required distances to find the error of the effector positions.

The experimental setup is shown in Fig. 7. The distances in the x and y directions were measured using the digital dial gauge with a measuring range of 0–80 mm and accuracy of ±0.001 mm. The distance in the z direction was measured by a laser displacement sensor with a resolution of 1 μm that was installed on the effector.

In the experiments, the effector was travelled at three different feed rates—50 mm/s, 100 mm/s and 200 mm/s—and different distances—±10 mm, ±30 mm and ±60 mm. The tests were performed 50 times in each moving direction. The average values of the measured distances and the errors are shown in Table. 1.
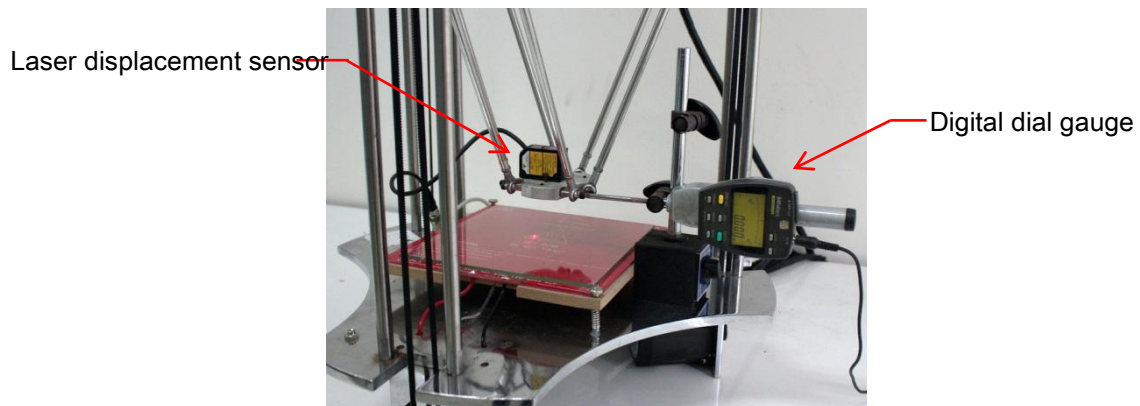

Fig. 7. Distance measurement setup.

The results show that the error of the robot position increases with increasing travel distance and feed rate. For example, consider the movement in the x direction at a feed rate of 50 mm/s; when the distance is increased from 10 mm to 60 mm, the error increases from 0.033 mm to 0.077 mm. Also consider the movement in the x- direction at the distance of 30 mm; when the feed rate is increased from 50 mm/s to 200 mm/s, the error increases from 0.052 mm to 0.607 mm. This is to be expected because an increased distance and feed rate results in an increasing quantisation error of the pulse rate computed for each motor. The average value of the error at the feed rates of 50 mm/s, 100 mm/s and 200 mm/s is 0.037 mm, 0.064 mm and 0.510 mm, respectively.

Table 1: Measured distances at different travel parameters

Direction	Feed 50 mm/s Distance (mm)			Feed 100 mm/s Distance (mm)			Feed 200 mm/s Distance (mm)		
	±10	±30	±60	±10	±30	±60	±10	±30	±60
X	10.033	30.052	60.077	10.062	30.078	60.136	10.347	30.607	60.928
	-10.031	-30.054	-60.075	-10.064	-30.073	-60.135	-10.351	-30.606	-60.931
Y	10.032	30.055	60.074	10.066	30.083	60.132	10.369	30.612	60.933
	-10.032	-30.054	-60.075	-10.065	-30.081	-60.133	-10.370	-30.611	-60.932
Z	10.001	30.004	60.006	10.003	30.007	60.010	10.087	30.263	60.881
	-10.000	-30.004	-60.005	-10.003	-30.008	-60.012	-10.089	-30.265	-60.884

In addition, based on observation, the travel paths determined in the experiments show that although the effector was required to travel on the x-y plane with a fixed z-value; the z-value of the effector was not constant but varied across the travel path. For example, consider the actual travel path of the effector, which travelled a distance of 60 mm in the x direction. At the beginning of travelling, the z-value was 0 mm but decreased to -1.94 mm (see Fig. 8) when the effector was located at the middle of the travel path. After that, it increased back to 0 mm when the effector reached the end position. This is because the kinematics of the mechanism are nonlinear in nature; that is, the kinematics are in sphere equation with the radius of L, as represented in Eqs. (5) - (7). Consequently, the actual travel path of the end effector was not straight but concavely curved.
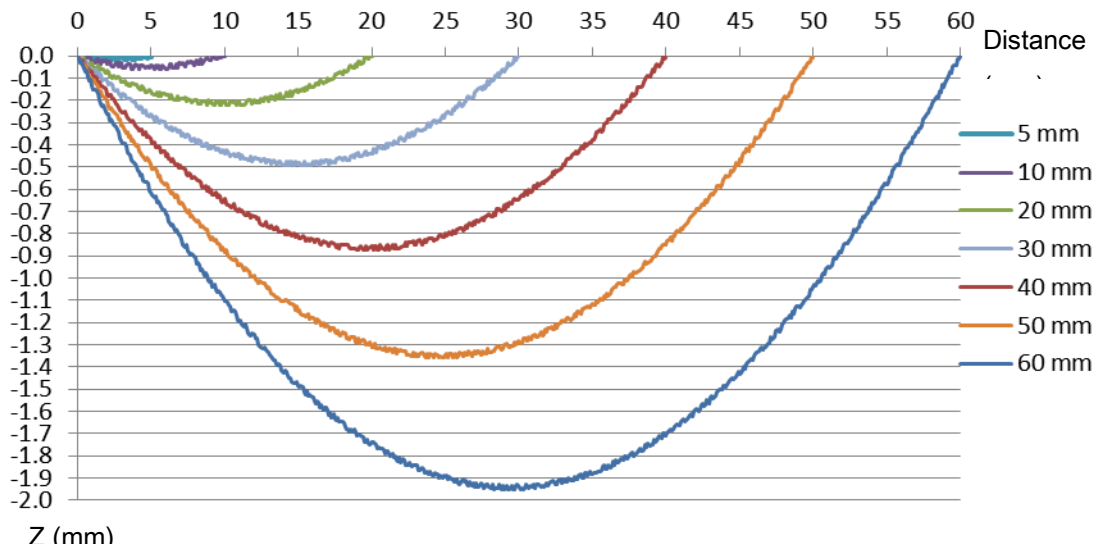

Fig. 8. The actual travel path of the end-effector at different distances.

However, in the FDM process, the z-value of the nozzle has to be constant to produce a straight layer. Therefore, it is necessary to investigate the technique of controlling the robot to reduce the variation in the z-value of the effector as it is travelling.

Based on the tests, when the effector travels a shorter distance, the variation of the z-value becomes smaller. For example, the deviation in the z-value decreased from -1.94 mm to -0.03 mm when the travel distance was reduced from 60 mm to 5 mm (Fig. 8).

Therefore, to reduce the variation in the z-value, the effector has to travel within a shorter distance. This can be done by dividing the travel path into small segments. The length of each segment depends on the allowable variation in the z-value. The example of travel paths experimentally obtained using different lengths of segment is illustrated in Fig. 9.
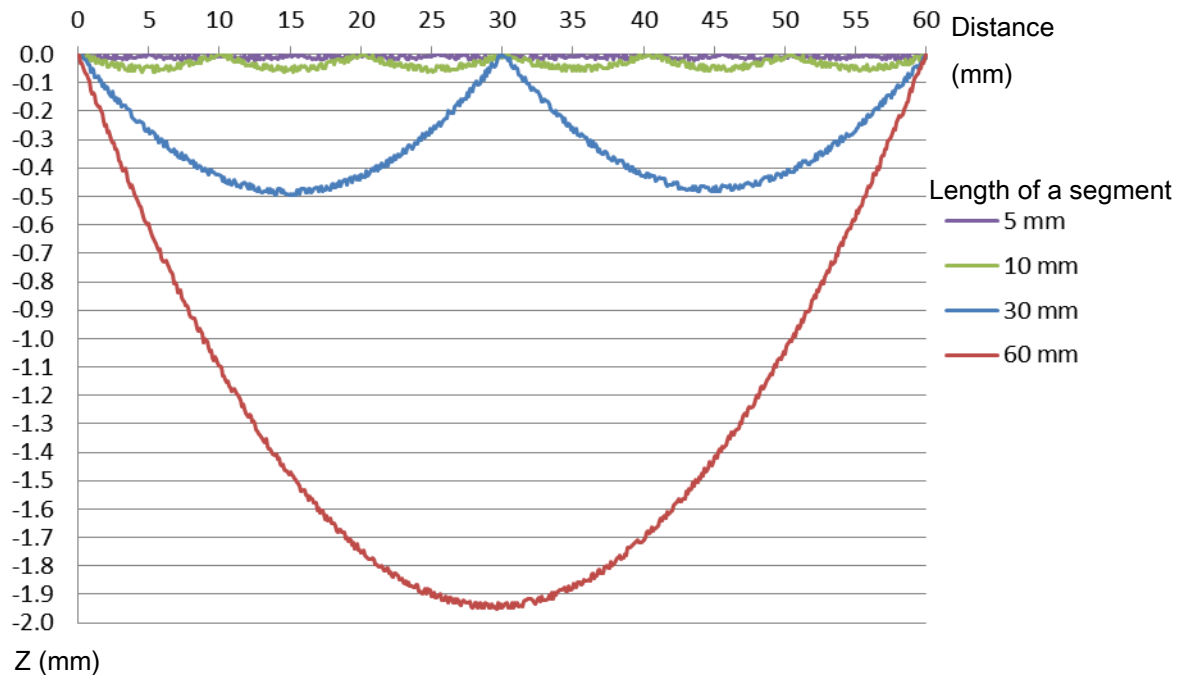
Fig. 9. The actual path of the effector travelling a distance of 60 mm in the x-direction on different segment lengths.

7. EXPERIMENTAL TESTS

To demonstrate that the developed robot system can produce real objects, four thin-wall objects having different shapes—square, cylindrical, square-based pyramid and rounded gear shapes (Fig. 10.)—were fabricated. The CAD models and dimensions of the models are shown in Figs. 10(a) to 10(d).
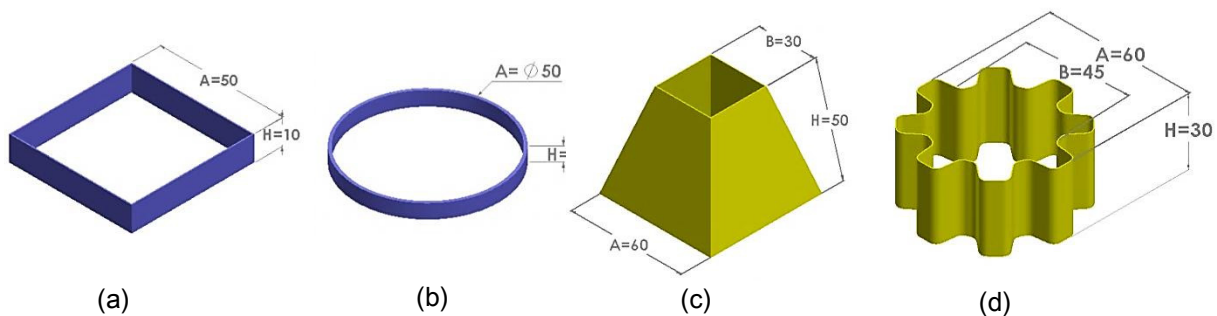
Fig. 10. 3D model of (a) square, (b) cylindrical, (c) square-based pyramid and (d) rounded gear.

The conditions of fabricating are that a layer thickness is 0.2 mm and a feed rate is 50 mm/min. In the tests, the variation in z-value was set to not be greater than the layer thickness. Therefore, the length of segment was selected to be 5 mm, which results in a maximum variation in the z-value of 0.03 mm.

To fabricate the parts precisely, the CAD models must be offset by a distance of a half of a layer width into the model. Based on preliminary tests, at the fabricating condition, the average width of a layer is about 0.19 mm. Therefore, the value of 0.08 mm (0.19/2=0.08 mm) was used as the offset distance. The tool paths were created from the offset profiles. The final parts of each shape are shown in Figs. 11 (a) - (d).

The dimensions of the actual parts were measured and compared with nominal values from CAD models to assess the fabricating accuracy. These were the width (A and B) and the height (H) of the parts (see Figs. 10(a) -10(d)). They were measured using digital Vernier calliper with accuracy of ±0.001 mm. All measurements were performed five times. The nominal and average actual values of the dimensions as well as standard deviation (SD) of the measurements are shown in Table. 2.

The value of dimensions of the actual parts and CAD models are close. The average errors of fabrication objects with the square, cylindrical, square pyramid and rounded gear shapes are 0.042 mm, 0.057 mm, 0.068 mm and 0.094 mm, respectively.

Although the actual parts were built from tool paths that were offset from the CAD models, there are errors in the dimensions between the parts and CAD models. This is because in the FDM process, there are other factors that affect the dimensional precision, such as nozzle and extrusion feed rate, layer thickness, temperature of the building platform and the filament heater. Therefore, to increase the accuracy of fabrication parts by the FDM process, these factors have to be investigated.
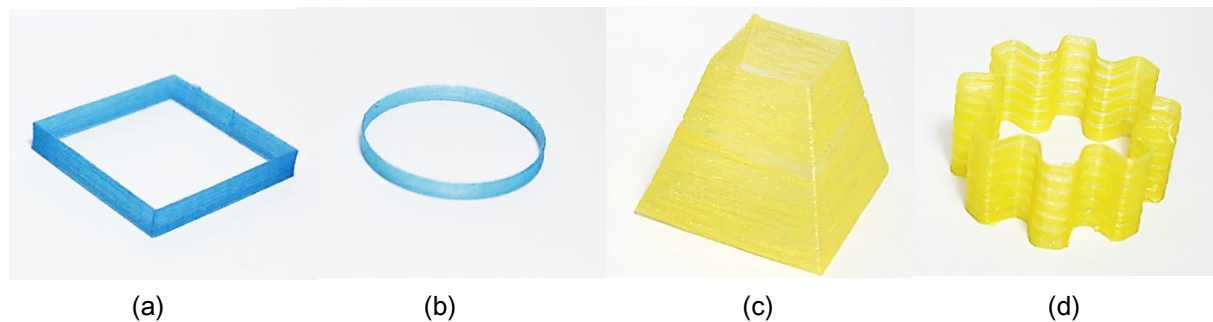
Fig. 11. Final parts of the (a) square, (b) cylindrical, (c) square-based pyramid and (d) rounded gear.

Table 2: CAD and measured values of dimensions of thin-wall objects

	A (mm)				H (mm)				B (mm)			
	Nominal	Actual	SD	Error	Nominal	Actual	SD	Error	Nominal	Actual	SD	Error
Square	50	50.042	0.011	0.042	10	10.004	0.002	0.004	-	-	-	-
Cylindrical	50	50.057	0.019	0.057	5	5.002	0.003	0.002	-	-	-	-
Square pyramid	60	60.068	0.016	0.068	50	50.058	0.004	0.058	30	30.021	0.019	0.021
Rounded gear	60	60.089	0.023	0.089	30	30.024	0.003	0.024	45	45.094	0.047	0.094

8. CONCLUSION

In the paper, the design and construction of a new linear delta robot for use in fuse filament additive manufacturing were detailed. The inverse and forward kinematics of the manipulator were derived. The parameters of the robot were optimised based on the kinematic equations and condition number in the required workspace. Repeatability tests were performed to evaluate the accuracy of the robot system. The investigation of the travel path of the effector showed that the effector should travel within a short distance so that the variation in z-value will be reduced. To demonstrate the capabilities of the developed robot system, components with four different shapes were produced. The results reveal that the robot can complete fabrication objects using the FDM process.

REFERENCES

[1]   Chua, C.K., Leong, K.F. and Lim, C.S. Rapid Prototyping: Principles and Applications, 2003, World Scientific Publishing, Singapore.

[2]   Choia, J.W., Medinaa, F., Kim, C., Espalin, D., Rodriguez, D., Stucker, B. and Wicker, R. Development of a mobile fused deposition modeling system with enhanced manufacturing flexibility, Journal of Materials Processing Technology, Vol. 211(3), 2011, pp. 424-432.

[3]   Lee, W.C., Wei, C.C. and Chung, S.H. Development of a hybrid rapid prototyping system using low-cost fused deposition modeling and five-axis machining, Journal of Materials Processing Technology, Vol. 214 (11), 2014, pp. 2366-2374.

[4]   Song, X., Pan, Y. and Chen, Y. Development of a low-cost parallel kinematic machine for multidirectional additive manufacturing, Journal of Manufacturing Science and Engineering, Vol. 137(2), 2015, pp. 297-310.

[5]   David Espalin. Development of a multi-material, multi-technology FDM system for process improvement experimentation, Dissertations, University of Texas, El Paso, 2012.

[6]   Iwan, Z., Dietmar, W.H., Kim, C.T. and Swee, H.T. Fused deposition modeling of novel scaffold architectures for tissue engineering applications, Biomaterials, Vol. 23(4), 2002, pp. 1169-1185.

[7]   Allahverdi, M., Danforth, S. C., Jafari, M. and Safari, A. Processing of advanced electroceramic components by fused deposition technique, Journal of the European Ceramic Society, Vol. 21 (10-11), 2001, pp. 1485-1490.

[8]   Mireles, J., Kim, H.C., Lee, I.H., Espalin, D., Medina, F., MacDonald, E. and Wicker, R. Development of a fused deposition modeling system for low melting temperature metal alloys, Journal of Electronic Packaging Transactions of the ASME, Vol. 135(1), 2013, [011008].

[9]   Dudek, P. FDM 3D printing technology in manufacturing composite elements, Archives of Metallurgy and Materials, Vol. 58(4), 2013, pp. 1415-1418.

[10] Ilardo, R. and Williams C.B. Design and manufacture of a formula SAE intake system using fused deposition modeling and fiber-reinforced composite materials, Rapid Prototyping Journal, Vol. 16(3), 2010, pp. 174-179.

[11] Vashishtha, V.K., Makade, R. and Mehla, N. Advancement of rapid prototyping in aerospace industry - a review, International Journal of Engineering Science and Technology, Vol. 3(3), 2011, pp. 2486-2493.

[12] Tellisa, B.C., Sziveka, J.A., Blissa C.L., Margolisa, D.S., Vaidyanathanb, R.K. and Calvertc, P. Trabecular scaffolds created using micro CT guided fused deposition modeling, Materials Science and Engineering: C, Vol. 28(1), 2009, pp. 171-178.

[13] Ultimaker 3D printer, URL: https://ultimaker.com, accessed on 15/04/2017.

[14] Makerbot 3D printer, URL: https://www.makerbot.com, accessed on 15/04/2017.

[15] Prusa 3D printer, URL: http://www.prusa3d.com, accessed on 15/04/2017.

[16] Seemecnc 3D printer, URL: https://www.seemecnc.com, accessed on 15/04/2017.

[17] Deltamaker 3D printer, URL: http://www.deltamaker.com, accessed on 15/04/2017.

[18] Allen, R. and Trask, R. An experimental demonstration of effective Curved Layer Fused Filament Fabrication utilising a parallel deposition robot, Additive Manufacturing, Vol. 8, 2015, pp. 78-87.

[19] Huang, B. and Singamneni, S. Alternate slicing and deposition strategies for fused deposition modeling of light curved parts, Journal of Achievements in Materials and Manufacturing Engineering, Vol. 55(2), 2012, pp. 511-517.

[20] Liu, X.J., Wang, J.S., OH, K.K. and Kim, J.W. A New Approach to the Design of a DELTA Robot with a Desired Workspace, Journal of Intelligent and Robotic Systems, Vol. 39(2), 2004, pp. 209-225.

[21] Liu, X.J. Optimal kinematic design of a three translational DoFs parallel manipulator, Robotica, Vol. 24(2), 2006, pp. 239-250.